

Evolution of a Quasi-Linear Convective System Sampled by Phased Array Radar

JENNIFER F. NEWMAN

School of Meteorology, University of Oklahoma, Norman, Oklahoma

PAMELA L. HEINSELMAN

NOAA/OAR/National Severe Storms Laboratory, and School of Meteorology, University of Oklahoma, Norman, Oklahoma

(Manuscript received 22 December 2011, in final form 21 May 2012)

ABSTRACT

On 2 April 2010, a quasi-linear convective system (QLCS) moved eastward through Oklahoma during the early morning hours. Wind damage in Rush Springs, Oklahoma, approached (enhanced Fujita) EF1-scale intensity and was likely associated with a mesovortex along the leading edge of the QLCS. The evolution of the QLCS as it produced its first bow echo was captured by the National Weather Radar Testbed Phased Array Radar (NWRT PAR) in Norman, Oklahoma. The NWRT PAR is an S-band radar with an electronically steered beam, allowing for rapid volumetric updates (~ 1 min) and user-defined scanning strategies. The rapid temporal updates and dense vertical sampling of the PAR created a detailed depiction of the damaging wind mechanisms associated with the QLCS. Key features sampled by the PAR include microbursts, an intensifying midlevel jet, and rotation associated with the mesovortex. In this work, PAR data are analyzed and compared to data from nearby operational radars, highlighting the advantages of using high-temporal-resolution data to monitor storm evolution.

The PAR sampled the events preceding the Rush Springs circulation in great detail. Based on PAR data, the midlevel jet in the QLCS strengthened as it approached Rush Springs, creating an area of strong midlevel convergence where it impinged on the system-relative front-to-rear flow. As this convergence extended to the lower levels of the storm, a preexisting azimuthal shear maximum increased in magnitude and vertical extent, and EF1-scale damage occurred in Rush Springs. The depiction of these events in the PAR data demonstrates the complex and rapidly changing nature of QLCSs.

1. Introduction

A disproportionately large fraction of violent tornadoes are spawned by supercell thunderstorms (e.g., Doswell 2001); however, a significant number of tornadoes are associated with other weather events, such as quasi-linear convective systems (QLCSs). Trapp et al. (2005) found that 18% of all tornadoes during a 3-yr period occurred within lines, as opposed to supercells or other phenomena such as tropical systems. Furthermore, Trapp et al. (2005) discovered a temporal bias in QLCS tornadoes. While the occurrence of both supercell and QLCS tornadoes peaked at approximately 1800 local time (LT), QLCS tornado occurrence displayed a secondary peak

during the late night and early morning hours, coincident with the tendency for linear storm systems to form after sunset (e.g., Maddox 1983). Since the public is less aware of severe weather warnings at night (e.g., Ashley et al. 2008), this secondary peak in QLCS tornado occurrence presents a significant risk. Furthermore, many nocturnal tornadoes occur without official National Weather Service (NWS) warning, due, in part, to a lack of visual observations (Brotzge and Erickson 2010).

Although QLCS tornadoes tend to be fairly weak, they can reach Fujita scale 2 (F2) intensity (Fujita 1971) and cause thousands of dollars in damage (Trapp et al. 2005). QLCS tornadoes can form in many locations along a squall line, presenting a challenge for forecasters trying to issue warnings. In addition, QLCS tornadoes do not typically produce a descending velocity signature in radar data (Trapp et al. 1999). Not surprisingly, it has been suggested that many unwarned tornadoes are associated with linear systems (Brotzge and Erickson 2010).

Corresponding author address: Jennifer F. Newman, School of Meteorology, University of Oklahoma, 120 David L. Boren Blvd., Norman, OK 73072.
E-mail: jennifer.newman@ou.edu

On 2 April 2010, the National Weather Radar Testbed Phased Array Radar (NWRT PAR, hereafter PAR) in Norman, Oklahoma, sampled a low-level circulation associated with a QLCS during the early morning hours. The Forecast Office in Norman did not classify this event as a tornado, primarily because only a large-scale (~2-km diameter) circulation was sampled by a nearby high-range-resolution X-band radar (KRSP; Junyent et al. 2010); this circulation served to enhance the strong surface winds of the QLCS, but was not considered to fit the classic definition of a tornado (D. L. Andra 2011, personal communication). However, these enhanced surface winds coincided with (enhanced Fujita) EF1-intensity damage (e.g., McDonald et al. 2004) in Rush Springs, Oklahoma, as assessed by an independent survey team [(Severe Hazards Analysis and Verification Experiment) SHAVE 2010].

In addition to the PAR research radar, two operational radars sampled the event: the Weather Surveillance Radar-1988 Doppler (WSR-88D) in Twin Lakes, Oklahoma (KTLX), and the Terminal Doppler Weather Radar (TDWR) in Norman, Oklahoma. The availability of radar data with different frequencies and resolutions allows for a unique dataset with opportunity for comparison. The location of all three central Oklahoma radars, in addition to the approximate path of the Rush Springs circulation, is shown in Fig. 1. The Rush Springs circulation was also sampled by one of the Collaborative Adaptive Sensing of the Atmosphere (CASA) radars in southwestern Oklahoma, KRSP. The reader is referred to Mahale et al. (2012) for a discussion of the Rush Springs circulation as sampled by KRSP.

Much of the previous research regarding QLCS circulations was accomplished during the Bow Echo and Mesoscale Convective Vortex Experiment (BAMEX) in the early 2000s (Davis et al. 2004). BAMEX researchers utilized airborne radars, mobile wind profilers, and a variety of other mobile instruments to study the evolution and dynamics of bow echoes and mesoscale convective vortices. Radar data for BAMEX cases were primarily derived from two sources: airborne X-band radars and nearby WSR-88Ds. The availability of two airborne Doppler radar antennas allowed for dual-Doppler analyses. However, a major disadvantage of the Electra Doppler Radar (ELDORA) airborne radars was the time required to complete each leg of the scanning strategy (typically 12–13 min; Wakimoto et al. 2006a). The temporal resolution of WSR-88Ds is also a significant limitation and could preclude adequate sampling of QLCS circulations. Atkins et al. (2005) noted that several tornadoes produced in association with the 10 June 2003 St. Louis bow echo had lifetimes shorter than the time required for a typical WSR-88D volume scan.

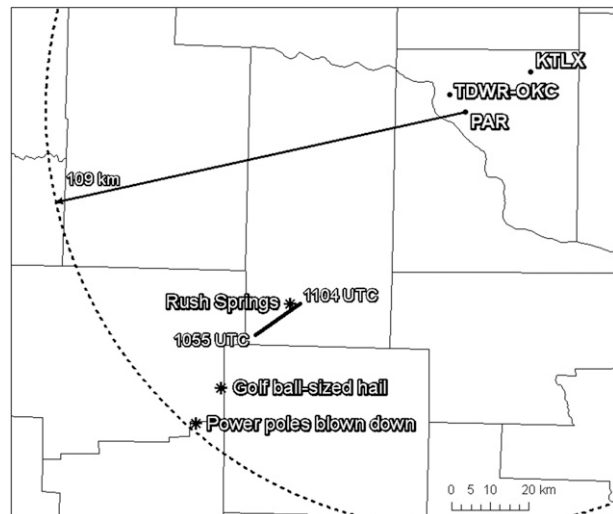


FIG. 1. Location of central Oklahoma radars discussed in the text. Path of Rush Springs circulation is denoted by thick black line, with approximate times as indicated. Wind and hail reports associated with the first microburst are also shown.

The PAR sampled the 2 April 2010 Rush Springs circulation with much higher temporal resolution, completing volume scans approximately every 2 min, compared to every 4.5 min for a WSR-88D operating in precipitation mode. In addition, the PAR employed an oversampled scanning strategy to collect data for the event, providing dense sampling in the vertical direction. By utilizing high-spatial and temporal resolution, the PAR was able to sample the evolution of the Rush Springs circulation and the pulselike nature of the QLCS in great detail. Analysis of the PAR data suggests that significant changes in QLCSs can occur on time scales of 2 min or less, and that, as a result, some features of QLCSs are likely not currently resolved by operational radars.

This work focuses on the evolution of the QLCS near Rush Springs as sampled by PAR. Several rapidly evolving features within the QLCS appeared to affect the strength and formation of the Rush Springs circulation, including a microburst, a strengthening midlevel jet, and gust front convergence. The evolution of these features is primarily examined using data from the PAR. In addition, comparisons are made to data collected by the other radars in central Oklahoma, showing the advantages of using rapid-scan volumetric radar data to detect significant changes in storm systems.

2. Review of QLCS circulations

Many mature QLCSs contain a strong rear-inflow jet (RIJ; e.g., Smull and Houze 1987), a region of enhanced winds that travel from the rear to the front of the system in the low to midtroposphere. The RIJ forms when

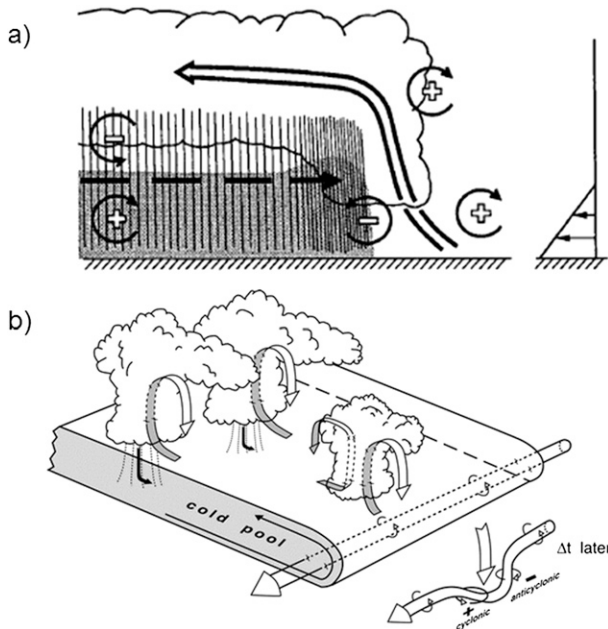


FIG. 2. (a) Final stage in the formation of an idealized bow echo. Circles with arrows indicate the sense of environmental and baroclinic vorticity. Black lines in bottom-right corner of figure indicate environmental vertical wind shear. Vertical lines indicate precipitation and shaded area indicates cold pool. Solid white line denotes front-to-rear flow and black dotted line denotes rear-to-front inflow. From Weisman (1992). (b) Conceptual model of mesovortex generation along outflow boundary of 5 Jul 2003 Omaha bow echo. The vortex tube in the bottom right shows how a downdraft-tilted baroclinically generated vorticity, forming a vertical vorticity couplet. The vortex tube is oriented in a north-south direction and is directed toward the south. From Wakimoto et al. (2006b).

updrafts are tilted upshear over the cold pool and air from the rear of the storm is accelerated downshear. The effects of baroclinically, cold pool-generated vorticity, and vorticity generated by the updraft-induced horizontal buoyancy gradient, combine to accelerate air through the cold pool toward the front of the storm (Fig. 2a).

Initially, damaging wind associated with QLCSs was attributed to the descent of the RIJ to the surface (e.g., Smull and Houze 1987). Detailed WSR-88D analyses and damage surveys indeed reveal large swaths of damage collocated with the RIJ in several bow echoes (e.g., Wheatley et al. 2006). Other studies have found areas of divergent damage associated with downbursts and microbursts along the line of storms (Forbes and Wakimoto 1983). However, many damage surveys have also revealed smaller, convergent, more intense areas of damage located within or outside the main damage swath (e.g., Fujita 1978, 1981; Forbes and Wakimoto 1983). Based on numerical simulations, Weisman and Trapp (2003) and Trapp and Weisman (2003) propose that meso- γ -scale vortices, or mesovortices within the bow echo are

responsible for these narrow areas of damage. Several radar-based studies have confirmed the existence of damage-producing mesovortices in QLCSs (e.g., Atkins et al. 2005; Wakimoto et al. 2006a; Wheatley et al. 2006).

Trapp and Weisman (2003) suggest that vorticity couplets form within bow echoes (preferentially north of the bow apex) when baroclinically generated vorticity at the leading edge of the cold pool is tilted downward by subsystem-scale downdrafts and subsequently stretched, increasing the resulting vertical vorticity magnitude. When a vortex line associated with the cold pool baroclinic vorticity is tilted downward, an anticyclonic vorticity maximum forms north of the downdraft and a cyclonic vorticity maximum forms south of the downdraft. In the Trapp and Weisman (2003) simulations, the cyclonic vorticity maximum eventually dominated as a result of the stretching of planetary vorticity.

The Trapp and Weisman (2003) mesovortex formation hypothesis was confirmed by Wakimoto et al. (2006b), who used an airborne radar to complete a Doppler wind synthesis of a bow echo on 5 July 2003. However, while Trapp and Weisman (2003) propose that a precipitating downdraft is the tilting mechanism in mesovortex formation, Wakimoto et al. (2006b) speculate that a mechanically forced downdraft (e.g., Heymsfield and Schotz 1985) was responsible for vorticity tilting in the 5 July 2003 case. A schematic model illustrating this mesovortex genesis process is shown in Fig. 2b.

Atkins and St. Laurent (2009) suggest slightly different mesovortex genesis mechanisms. In quasi-idealized simulations of a bow echo on 10 June 2003 (see Atkins et al. 2005), both cyclonic vortices and cyclonic-anticyclonic vortex couplets were observed. The cyclonic-only vortices were observed to form at all stages of bow echo evolution. Atkins and St. Laurent (2009) propose that these cyclonic vortices form when air descending roughly parallel to the gust front acquires the horizontal vorticity induced by the leading edge of the cold pool. This horizontal vorticity is subsequently tilted and stretched by an updraft along the gust front. In contrast, cyclonic-anticyclonic vortex couplets were primarily observed only during the early bow echo stage. In the simulations, a convective-scale downdraft produced strong outflow that created an outward bulge in the gust front. This outflow induced a new updraft, which tilted the vortex lines associated with the cold pool upward, creating a vorticity couplet.

As many aspects of QLCS mesovortices are still poorly understood, high-temporal-resolution sampling by the PAR could provide the opportunity to study these events in greater detail than what has previously been achieved with operational radars. Heinselman et al. (2008) showed that examining high-resolution PAR data made it easier

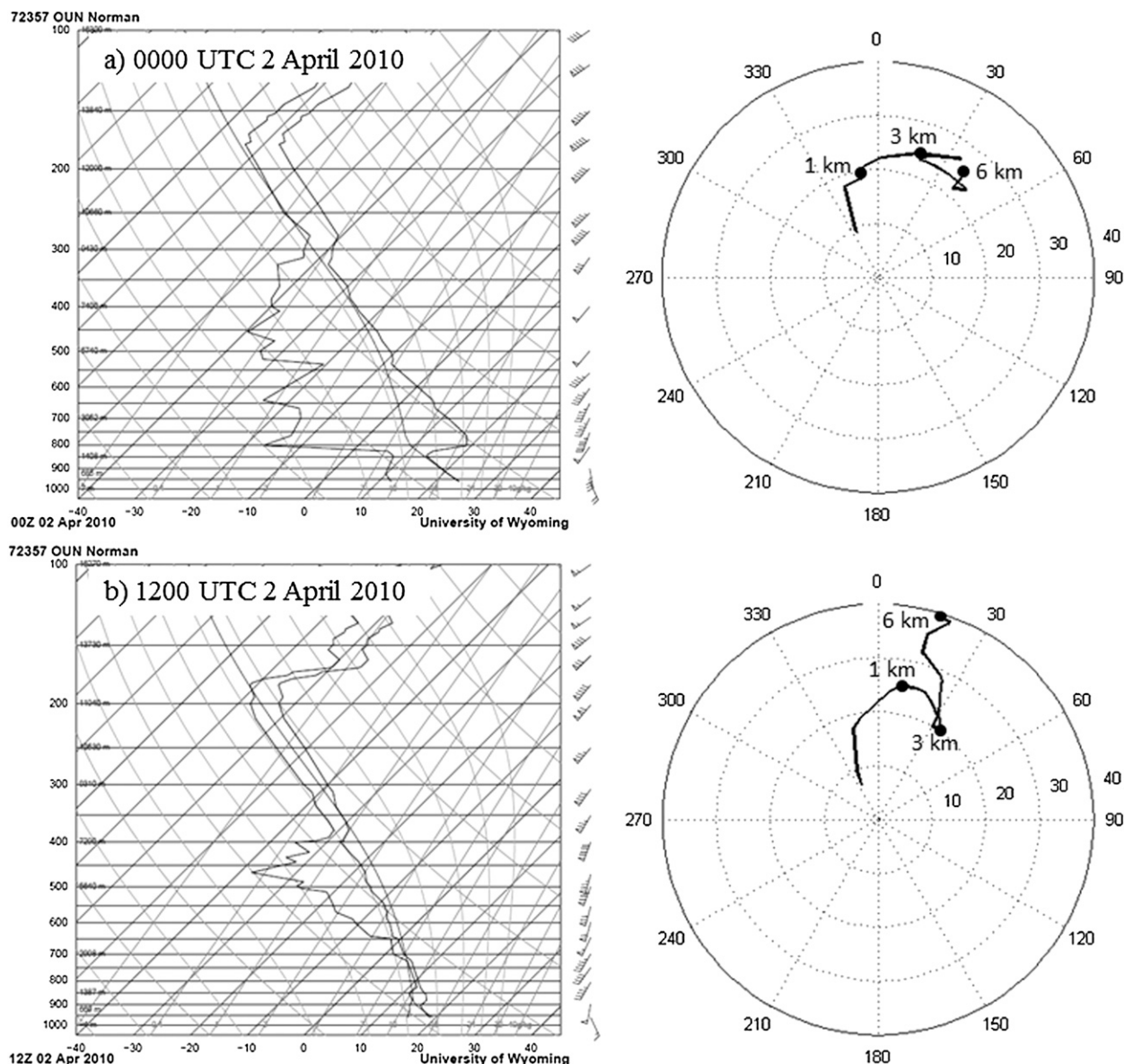


FIG. 3. (left) Soundings from (a) 0000 and (b) 1200 UTC 2 Apr 2010 from Norman, OK. Pressure is plotted in hPa and temperature is plotted in $^{\circ}\text{C}$. Wind barbs are shown in units of m s^{-1} , with one whole barb equal to 5 m s^{-1} and one pennant equal to 25 m s^{-1} . (right) Hodographs for wind observations in the lowest 6 km of soundings with wind speeds shown in m s^{-1} and small numbers indicating height above ground level.

to identify rapidly evolving dynamical features within weather systems, such as strengthening low-level convergence and vorticity associated with a reintensifying supercell. PAR data could potentially depict previously unresolved features of QLCSs and provide insight into the formation mechanisms of tornadic mesovortices.

3. Synoptic overview

The QLCS occurred during the early morning hours of 2 April 2010 as a strong cold front moved through

central Oklahoma. An upper-level trough also moved through Oklahoma overnight, adding to the cold frontal forcing. By 1200 UTC, wind speeds had increased considerably in response to the approaching cold front, increasing the speed shear significantly. In addition, backing winds ahead of the front increased low-level directional shear (see hodograph in Fig. 3b). Based on the 1200 UTC Norman, Oklahoma, sounding (Fig. 3b), the magnitude of the surface to 2.5-km wind shear was approximately 20 m s^{-1} . (This sounding was launched at 1100 UTC, so it approximately represents the prestorm environment.)

According to a numerical modeling study by Weisman and Trapp (2003), a low-level shear value of 20 m s^{-1} is sufficient for the formation of bow echoes and the development of strong mesovortices. However, caution must be used when making comparisons to these simulations. Weisman and Trapp (2003) used a unidirectional shear profile where wind speed increases linearly with height in the direction normal to the QLCS; the wind profile from the Rush Springs QLCS clearly does not fit this model (Fig. 3).

By 1200 UTC, the base of the trough was located in southern New Mexico, and much of western and central Oklahoma was located in a region of strong southwesterly mid- and upper-level flow associated with the eastern side of the trough. Because of a midlevel jet maximum, the wind speed increased substantially with height in the 0–6-km layer (Fig. 3b); as a result, the 0–6-km shear vector magnitude was nearly 40 m s^{-1} during the QLCS event. This shear value is sufficient for long-lived multicellular convection and supercell structures with midlevel rotation (Rasmussen and Blanchard 1998). The mixed-layer convective available potential energy (MLCAPE), calculated using the surface station pressure and the average temperature and mixing ratio in the lowest 100 hPa of the sounding, was 1304 J kg^{-1} from the 1200 UTC Norman sounding. This value is on the lower end of expected CAPE values for MCS or bow echo environments (e.g., Weisman 1993; Evans and Doswell 2001).

4. Event overview

As the upper-level trough approached from the west, storms began to form in northwest Texas, just south of the Oklahoma border, by 0600 UTC. Over the next several hours, these storms matured and moved eastward into a region of moderate instability. The 0900 UTC Storm Prediction Center mesoanalysis indicated a region of uncapped 1000 J kg^{-1} surface-based CAPE in central Oklahoma, near the location of Rush Springs (not shown). The isolated storms grew in both size and intensity as they moved into the narrow corridor of instability in southwestern Oklahoma. Between 0800 and 1000 UTC, the southern storms increased moderately in strength while additional storms formed rapidly farther north in Oklahoma. The storms in Texas moved northeastward into Oklahoma, forming a QLCS by 1030 UTC. The initial stages of the QLCS were sampled by KTLX only (Fig. 4a), as PAR data collection had not yet begun. Between 1055 and 1101 UTC, a bowing segment developed in the southern portion of the QLCS, causing significant wind damage in the Rush Springs area; this stage of the QLCS was sampled by the PAR (Fig. 4b) in addition to KTLX. The QLCS moved eastward through

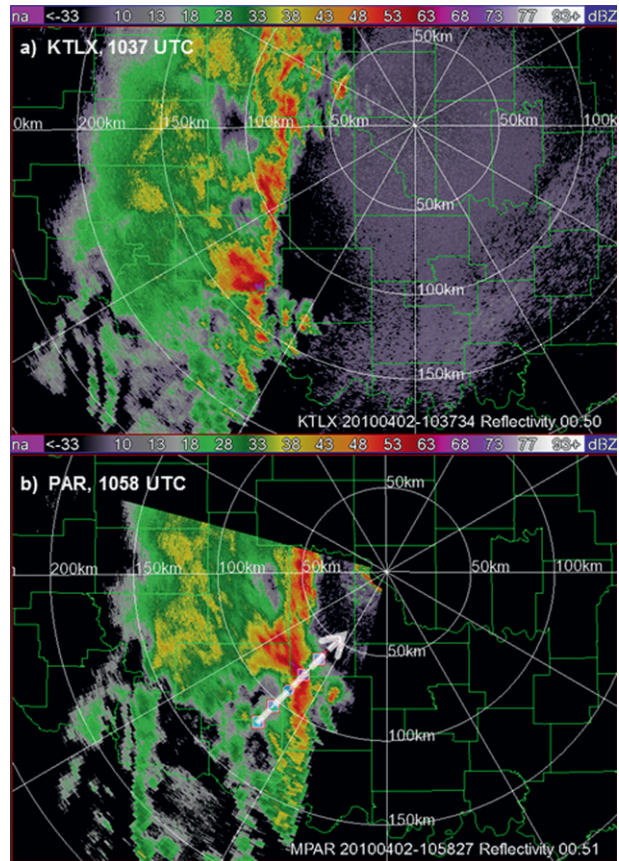


FIG. 4. (a) KTLX 0.5° reflectivity at 1037 UTC 2 Apr 2010. (b) PAR 0.5° reflectivity at 1058 UTC 2 Apr 2010. In (b), dashed line shows cross-sectional location discussed in PAR analysis section. In both images, Oklahoma counties are outlined in green, and range rings for each radar are shown in increments of 50 km.

Oklahoma and weakened during the early morning hours.

A damage survey of Rush Springs was led by Kiel Ortega, a research associate with the University of Oklahoma Cooperative Institute for Mesoscale Meteorological Studies. The damage survey team determined that the EF1-scale Rush Springs damage was associated with a circulation embedded along the leading edge of the QLCS (see Fig. 1 for damage path). Damage signatures included peeled roof shingles and several rolled-over mobile homes. Since the storm motion of the QLCS was very fast (at least 25 m s^{-1}), the true intensity of the Rush Springs circulation is unknown; the motion of the QLCS likely augmented the circulation intensity substantially.

5. PAR data analysis

PAR is an S-band (9.38 cm) research radar located in Norman, Oklahoma. Unlike a WSR-88D, the PAR

operates by using a panel of transmit/receive elements, changing the phases of the elements to steer the radar beam in azimuth and elevation. Electronic beam steering offers several potential advantages over conventional mechanical steering, including a 75% reduction in volumetric scan time (in comparison to a WSR-88D) and the ability to adaptively scan regions of interest (Zrnić et al. 2007; Heinselman and Torres 2011). The research PAR used for this study only has one panel of transmit/receive elements and therefore can only scan one 90° sector at a time (e.g., Fig. 4b). However, an operational PAR would have four panels that could simultaneously scan four 90° sectors at the same time, producing full volumetric updates in 1–2 min (Heinselman et al. 2008).

The transmitted beamwidth of the PAR increases gradually with increasing angle from boresight (the center of the panel), ranging from 1.5° at boresight to 2.1° at an angle of 45° from boresight. Overlapped azimuthal sampling is used, such that the sampling interval at a particular location is equal to one-half of the beamwidth at that location. The range resolution of the PAR is 240 m (Zrnić et al. 2007).

a. Sampling strategies

On 2 April 2010, the PAR was operating nearly continuously from 1037 to 1140 UTC, and during that time used two different scanning strategies. Initially, an over-sampled scanning strategy was employed, which collects data at 22 elevation angles and uses two different pulse repetition times (PRTs) at the lowest elevation angles to properly place range-folded echoes. At 1100 UTC, once the QLCS had moved within 120 km of the PAR, a different scanning strategy was employed. The second scanning strategy also collected data at 22 elevation angles, but a uniform PRT was used for all tilts, allowing for a faster update time. The average volumetric update times for the two scanning strategies were 2 and 1.4 min, respectively.

The Nyquist velocity of the PAR was 29.3 m s^{-1} during the event. Some wind speeds within the QLCS exceeded 30 m s^{-1} at low levels and 40 m s^{-1} at mid- and upper levels, surpassing the Nyquist velocity. To improve the depiction of velocity signatures within the QLCS, velocity data were de-aliased manually with the Solo II editing program (Oye et al. 1995).

b. Microburst

The first event sampled by the PAR (1037–1050 UTC) was a microburst ~110 km from the radar that resulted in estimated 30 m s^{-1} winds in Cotton County and knocked over several power poles [(National Climatic

Data Center) NCDC 2010]. Golf ball-sized hail also fell in association with the microburst (NCDC 2010). The location of the microburst damage reports is shown in Fig. 1; the evolution of the microburst as seen in the PAR data corresponds well spatially and temporally to these reports (Fig. 5).

When the PAR began collecting data at 1037 UTC, a high reflectivity core ($>65 \text{ dBZ}$), indicative of hail, had already elongated and started to descend toward the ground (Fig. 5a). The reflectivity core initially extended from the lowest PAR scan at ~1.7 km above radar level (ARL) to nearly 8 km ARL. According to an NCDC (2010) report, at approximately 1040 UTC, eight power poles were knocked down in Hulen, Oklahoma, as a result of an estimated 30 m s^{-1} wind gust. At this time, the reflectivity core associated with the microburst was still descending. By 1044 UTC, we estimate that the core had almost completely descended to the ground.

The 1044 UTC PAR velocity vertical cross section shows an elevated region of strong inbound velocities associated with a midlevel jet, centered near $z = 6 \text{ km}$ (Fig. 5d). In this cross section, a narrow region of high inbound velocities extends from the midlevel jet downward to the surface, creating a low-level wind maximum near $x = 110 \text{ km}$, just to the left (southwest) of the wind report in Fig. 5d. The magnitude of this maximum, measured at 1.6 km ARL by the PAR, was 30.3 m s^{-1} , which is quite close to the estimated wind gust speed in Hulen. In addition, this wind speed is very similar to the radial wind speeds measured in the midlevel jet by the PAR during this time period. Thus, it appears likely that high-momentum air was transferred downward from the midlevel jet toward the surface, possibly in conjunction with the microburst.

Golf ball-sized hail (~1.75-in. diameter) was reported at 1050 UTC near Bethel, Oklahoma (NCDC 2010). The location of this hail report corresponds well with the location of the reflectivity core at the end of the microburst's lifetime (Fig. 5f). Since the lowest elevation angle of the PAR was sampling the storm ~1.6 km ARL at this location, the high reflectivity core was not sampled as it reached the surface. However, based on the observations of the reflectivity core in the previous PAR cross sections, we suspect that the core reached the ground between 1044 and 1050 UTC, producing the golf ball-sized hail reported in Bethel.

c. Strengthening low-level outflow

The microburst that occurred between 1037 and 1050 UTC appeared to locally strengthen the outflow along the gust front (Fig. 6a). Soon after 1050 UTC, this area of strengthening outflow began to extend northwestward and southeastward along the QLCS (Figs. 6b–f).

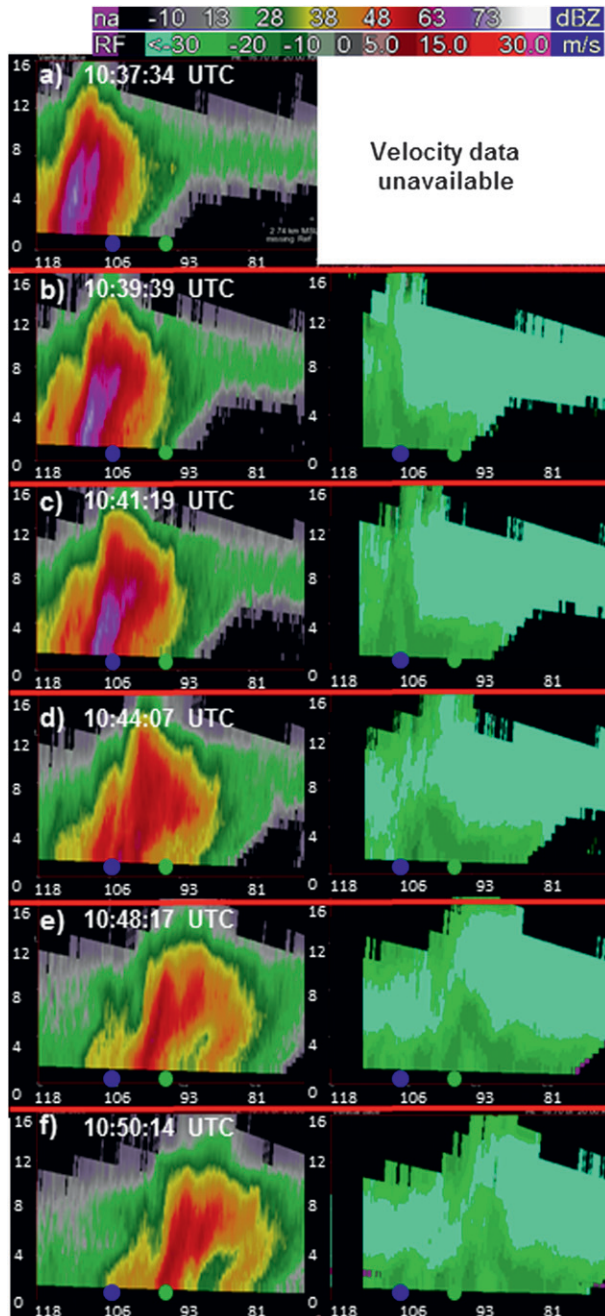


FIG. 5. (left) PAR northeast-southwest reflectivity and (right) velocity vertical cross sections. Location of cross section shown in Fig. 4. Decreasing numbers on the x axis indicate distance from the PAR in km. Blue and green circles denote approximate locations of wind and hail reports, respectively, as discussed in the text. (a) 1037:34, (b) 1039:39, (c) 1041:19, (d) 1044:07, (e) 1048:17, and (f) 1050:14 UTC 2 Apr 2010.

The reflectivity at the 0.5° elevation angle began to develop into a bowing structure in response to this surge of outflow, forming a well-defined bow segment by 1054 UTC (Fig. 6c).

Although the gust front of the QLCS was not indicated by a typical fine line in reflectivity imagery (e.g., Wilson et al. 1980), a sharp gradient was present in the 0.5° velocity field (Fig. 6). Several cyclonic azimuthal shear maxima were evident along the gust front; one particular azimuthal shear maximum, located on the north side of the intensifying outflow, persisted with time and began to strengthen at approximately 1058 UTC (Fig. 10). The strengthening of this shear maximum coincided with the formation of a notch in the reflectivity field (Fig. 6). (As discussed in later sections, this shear maximum was associated with the mesovortex that contributed to the damage in Rush Springs.) As the strong low-level outflow extended northwestward along the QLCS, the shear maximum increased in intensity, reaching a maximum value of 0.00729 s^{-1} at 1101 UTC (Fig. 10e). This maximum value occurred when the strong outflow had extended completely to the location of the shear maximum. Thus, it is likely that the mechanism that caused the outflow to strengthen along the QLCS also helped to strengthen the existing azimuthal shear maximum.

A series of vertical cross sections taken across different points of the strengthening outflow indicates that midlevel jet momentum was being transferred to the surface in a similar method to the momentum transfer that produced the wind gust in Hulen. An example of one of these cross sections is shown in Fig. 7 from 1050 to 1104 UTC. At 1052 UTC, a region of velocities exceeding 30 m s^{-1} extended from the bottom of the midlevel jet at $z \sim 6 \text{ km}$ toward the surface near $x = 93 \text{ km}$ (Fig. 7b). By 1104 UTC (8 min later), the extension between the midlevel jet and the area near the surface dissipated, but the high velocities at the lowest elevation angle remained (Fig. 7h). This process occurred at several locations along the QLCS as portions of the gust front strengthened and expanded.

The initial microburst at 1037 UTC was associated with the first in a series of downward momentum transfers that caused the low-level winds along the gust front to intensify with time. The importance of momentum transport in QLCSs was demonstrated by Mahoney et al. (2009); modeling results suggest that momentum transport can significantly increase surface winds and affect mesovortex strength.

d. Strengthening midlevel jet

Throughout the 2 April 2010 event, a southwesterly midlevel jet was prominent in Oklahoma, which affected the mid- and low-level flow within the QLCS. As discussed in the previous section, it is likely that momentum from this midlevel jet descended and strengthened the outflow at several locations along the gust front between 1050 and 1101 UTC. During this time period,

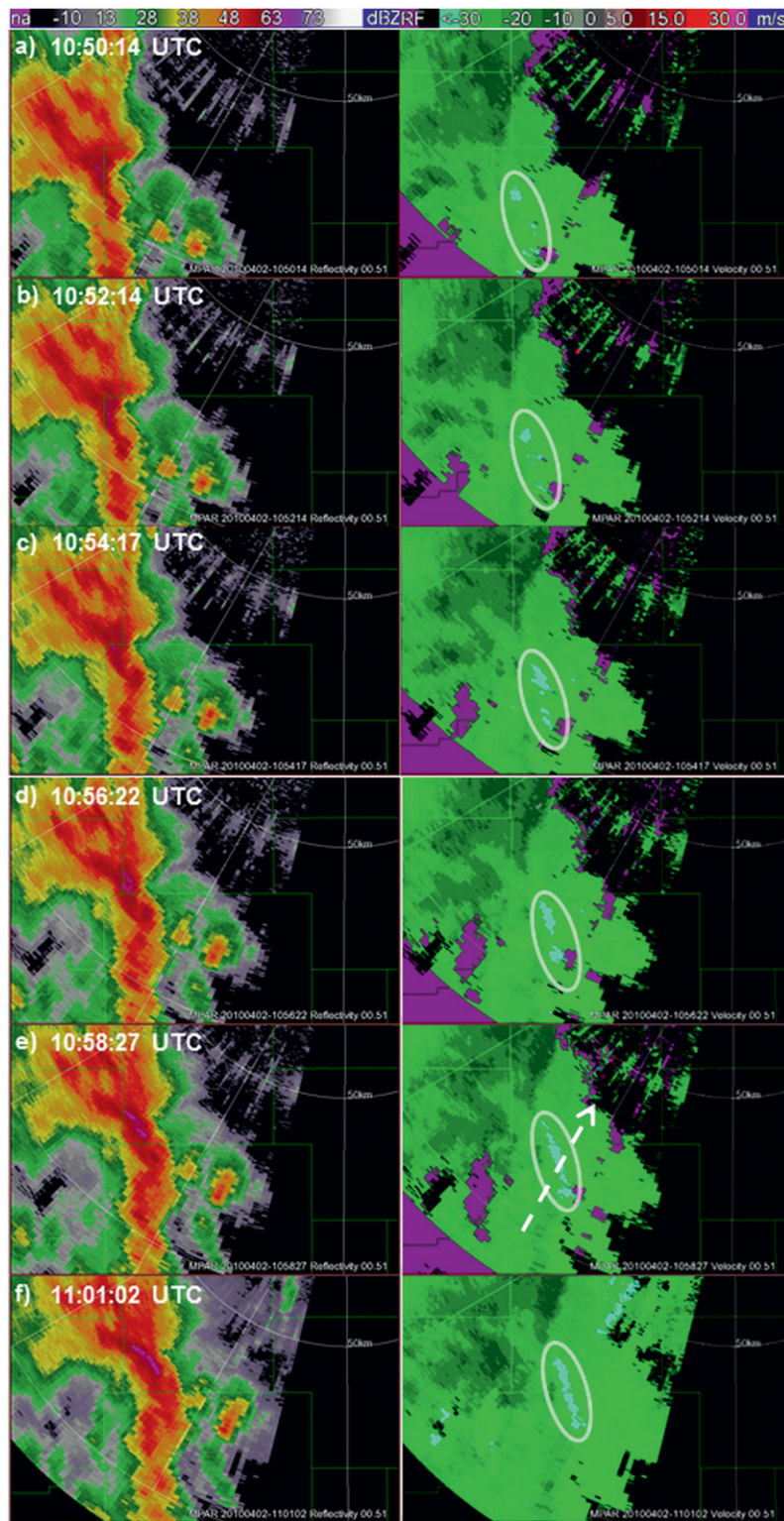


FIG. 6. (left) PAR 0.5° reflectivity and (right) velocity plan position indicator (PPI) scans. Oklahoma counties are outlined in green and range rings for the PAR are shown in increments of 50 km, with the first range ring corresponding to a range of 50 km. In velocity images, white circles indicate intensifying outflow. Radial spikes seen in images are the result of sidelobe echoes. (a) 1050:14, (b) 1052:14, (c) 1054:17, (d) 1056:22, (e) 1058:27, and (f) 1101:02 UTC. White arrow in (e) denotes location of cross section in Fig. 7.

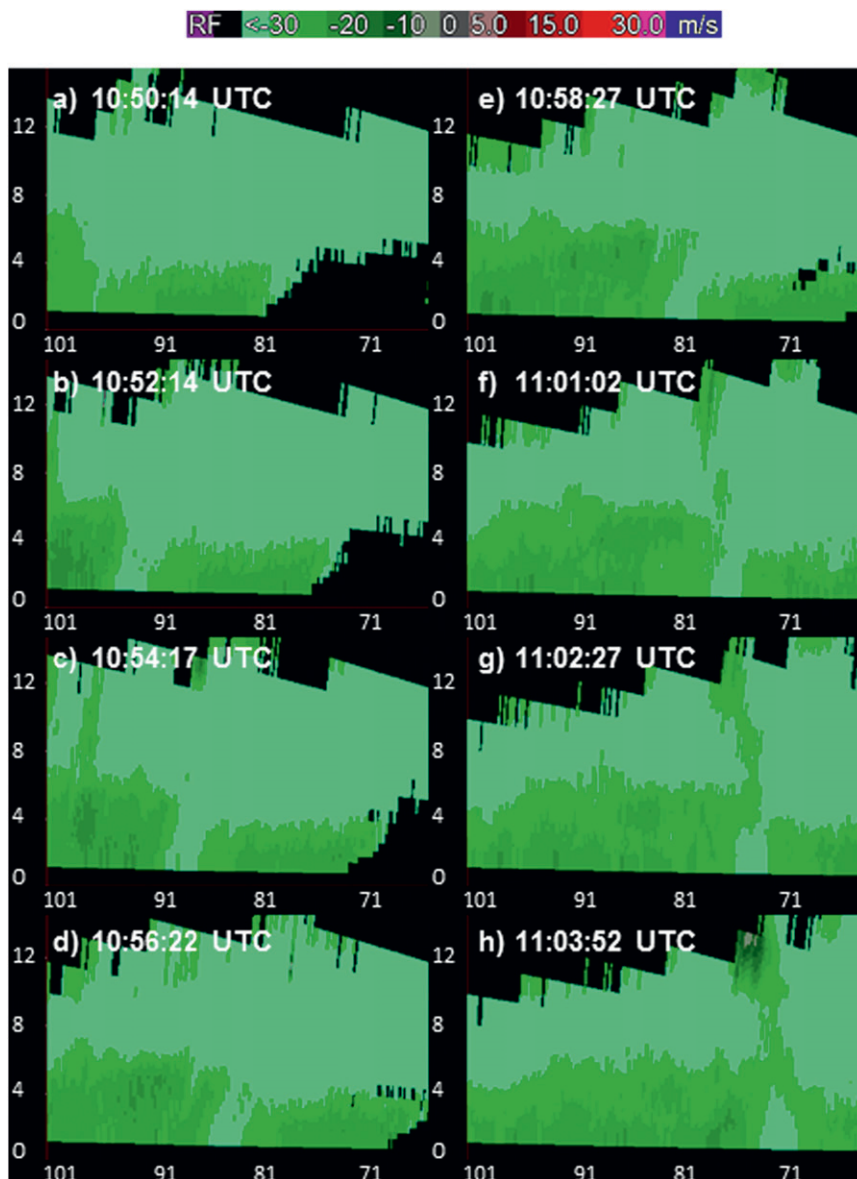


FIG. 7. PAR northeast-southwest velocity vertical cross sections. Decreasing numbers on the x axis indicate distance from the PAR in km. Location of cross section is shown in Fig. 6e.

the midlevel jet appeared to strengthen and expand in vertical extent.

Because of data quality issues related to range folding, the midlevel jet was not visible in the PAR data until 1048 UTC, centered at ~ 6 km above MSL with base velocities of 30 m s^{-1} (Fig. 5e). Initially, a small area of approaching storm-relative velocities was evident at midlevels; storm-relative velocity magnitudes were $5\text{--}8 \text{ m s}^{-1}$ in the outer regions of the jet and $10\text{--}12 \text{ m s}^{-1}$ in the narrow jet core. Between 1050 and 1052 UTC (Figs. 8a,b), the leading edge of the jet core increased noticeably in both strength and depth. By 1054 UTC

(Fig. 8c), a large region in the jet exhibited storm-relative velocities exceeding 10 m s^{-1} . By 1101 UTC (Fig. 8f), most storm-relative velocity magnitudes in the jet core were $11\text{--}14 \text{ m s}^{-1}$. The strengthening jet created an area of convergence where it met the front-to-rear inflow (e.g., near $x \sim 81 \text{ km}$, $z \sim 7 \text{ km}$ in Fig. 8e).

e. Mesovortex circulation

Since only a cyclonic vortex was observed in both PAR and CASA data (Mahale et al. 2012), as opposed to a vorticity couplet, a cyclonic vortex-only mesovortex genesis mechanism may have taken place, as discussed

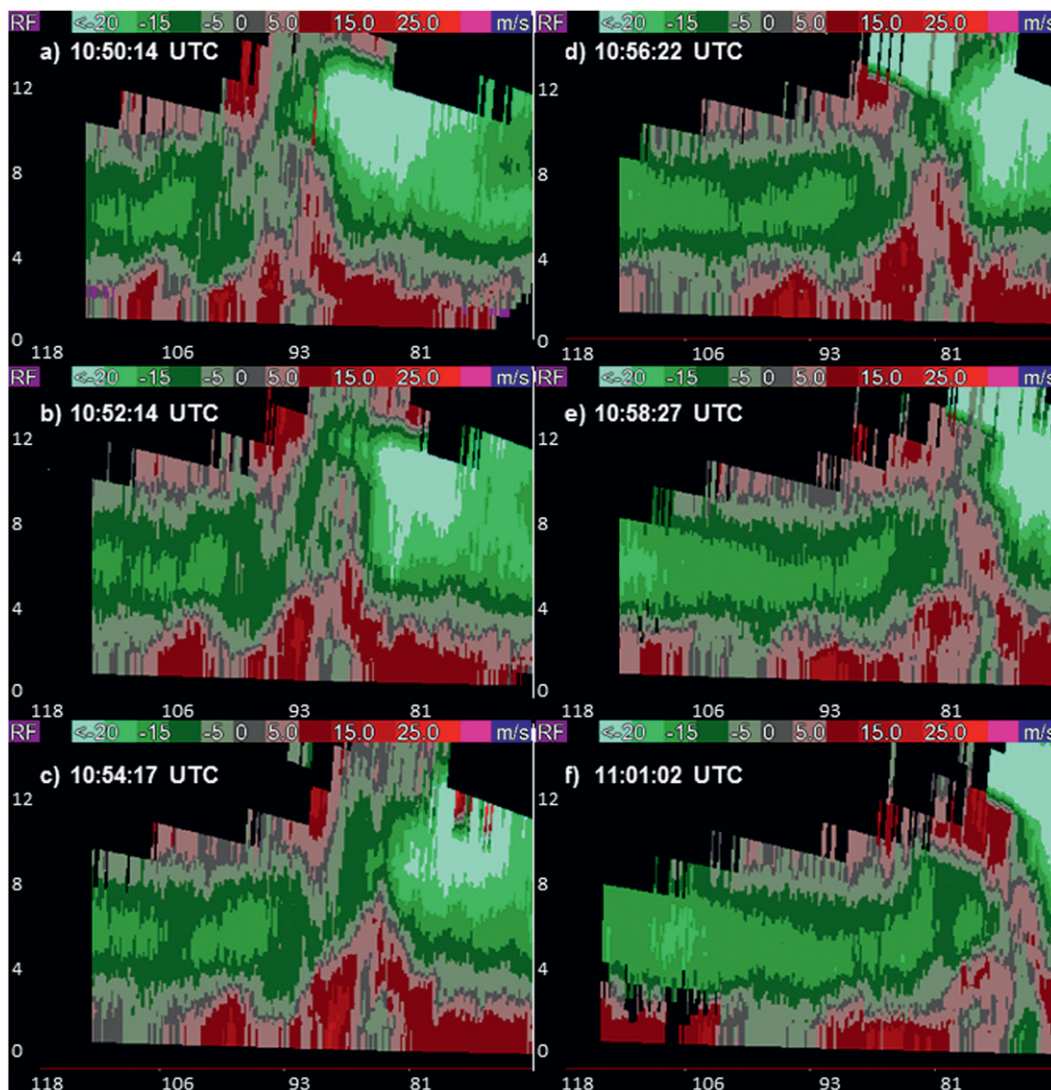


FIG. 8. PAR northeast-southwest storm-relative motion vertical cross section. Location of cross section shown in Fig. 4. Decreasing numbers on the x axis indicate distance from the PAR in km. (a) 1050:14, (b) 1052:14, (c) 1054:17, (d) 1056:22, (e) 1058:27, and (f) 1101:02 UTC.

in the background section (see also Atkins and St. Laurent 2009). Without the use of a numerical simulation or trajectory analysis, it is difficult to determine source regions for the mesovortex air parcels and the origin of the vertical vorticity associated with the mesovortex. However, the evolution of the azimuthal shear maximum associated with the circulation can still be examined using the available PAR data and related to the dynamics of the QLCS.

By 1102 UTC, a moderately strong velocity couplet (maximum velocity difference $\sim 20 \text{ m s}^{-1}$) associated with the mesovortex was evident in the 0.5° PAR storm-relative motion field (Fig. 9). At this time, the circulation was located $\sim 70 \text{ km}$ from the PAR and the

0.5° scan was sampling the circulation $\sim 0.9 \text{ km ARL}$. Similar to past studies of bow echo mesovortices (e.g., Atkins et al. 2005), the circulation was located just north of the bowing segment (Figs. 6 and 9).

An azimuthal shear cross section following the path of the developing velocity couplet from 1052 to 1104 UTC shows a low-level azimuthal shear maximum increase in vertical extent and magnitude (Figs. 10a-d), reaching a value of 0.00729 s^{-1} at 1101 UTC (Fig. 10e), before tilting downshear and weakening at low levels (Figs. 10f-g). The path of the low-level shear maximum agrees well with the circulation damage path. In addition, the fluctuations in the low-level shear magnitude correspond temporally to the development and dissipation of the

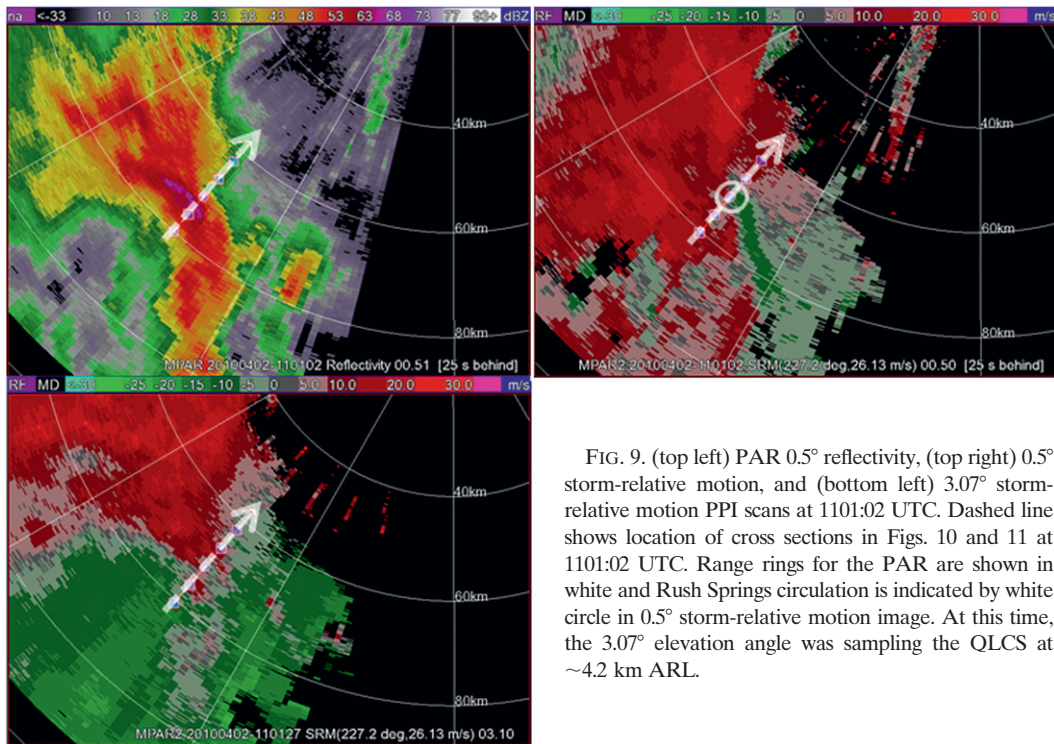


FIG. 9. (top left) PAR 0.5° reflectivity, (top right) 0.5° storm-relative motion, and (bottom left) 3.07° storm-relative motion PPI scans at 1101:02 UTC. Dashed line shows location of cross sections in Figs. 10 and 11 at 1101:02 UTC. Range rings for the PAR are shown in white and Rush Springs circulation is indicated by white circle in 0.5° storm-relative motion image. At this time, the 3.07° elevation angle was sampling the QLCS at ~ 4.2 km ARL.

circulation, as will be discussed in section 6d. The azimuthal shear vertical cross sections (Fig. 10) suggest that the circulation developed from the ground up, which is typical for some nonsupercell tornadoes and circulations (e.g., Wakimoto and Wilson 1989), particularly those that form in association with a QLCS (Trapp et al. 1999). This ground-up development is consistent with the tornadic mesovortices studied by Atkins et al. (2005).

f. Enhancement of mesovortex circulation

The strengthening of the midlevel jet and the low-level outflow coincided with the timing of mesovortex formation, indicated by the strengthening azimuthal shear maximum in the PAR data (Fig. 10). In this section, it is proposed that convergence associated with the strengthening midlevel jet served to enhance the existing mesovortex circulation embedded in the QLCS.

Figure 11 supports the comparison of the convergence field to the location of the jet from 1052 to 1104 UTC. [Damage was occurring in Rush Springs from 1055 to 1104 UTC based on high-resolution CASA data (Mahale et al. 2012) and damage signatures on the ground (SHAVE 2010). In Figs. 10 and 11, this approximately corresponds to the area from $X = 80$ to 65 km.] As the midlevel jet impinged on the front-to-rear system-relative flow, it created an area of midlevel convergence. We speculate that momentum and convergence associated with the jet

were transported downward (Fig. 11), which may have, in turn, enhanced the strength of the preexisting surface circulation through vertical vorticity stretching and vorticity convergence.

The Rush Springs mesovortex enhancement is depicted in the azimuthal shear cross sections in Fig. 10; the azimuthal shear maximum grows taller and narrower as it strengthens during this same time period. The proximity between this shear maximum and the jet is evident in Fig. 11e, where the area of strong rotation at the surface at $x = 70$ km appears to be located just underneath the leading edge of the midlevel jet. Near the low-level velocity couplet, an area of strong convergence extended from ~ 1 to 4 km ARL. This evolution suggests that the Rush Springs mesovortex was enhanced by the downward transport of momentum and convergence associated with the strengthening midlevel jet.

The relation between mesovortices and the RIJ has previously been explored for a case during the BAMEX project. In their study of the 10 June 2003 St. Louis bow echo, Atkins et al. (2005) noted that tornadic mesovortex genesis appeared to be associated with RIJ formation and descent. Atkins et al. (2005) suggest that the RIJ can create localized areas of convergence and strengthen the gust front, promoting stronger vertical vorticity stretching along the gust front and increasing the likelihood for mesovortex formation. This finding was

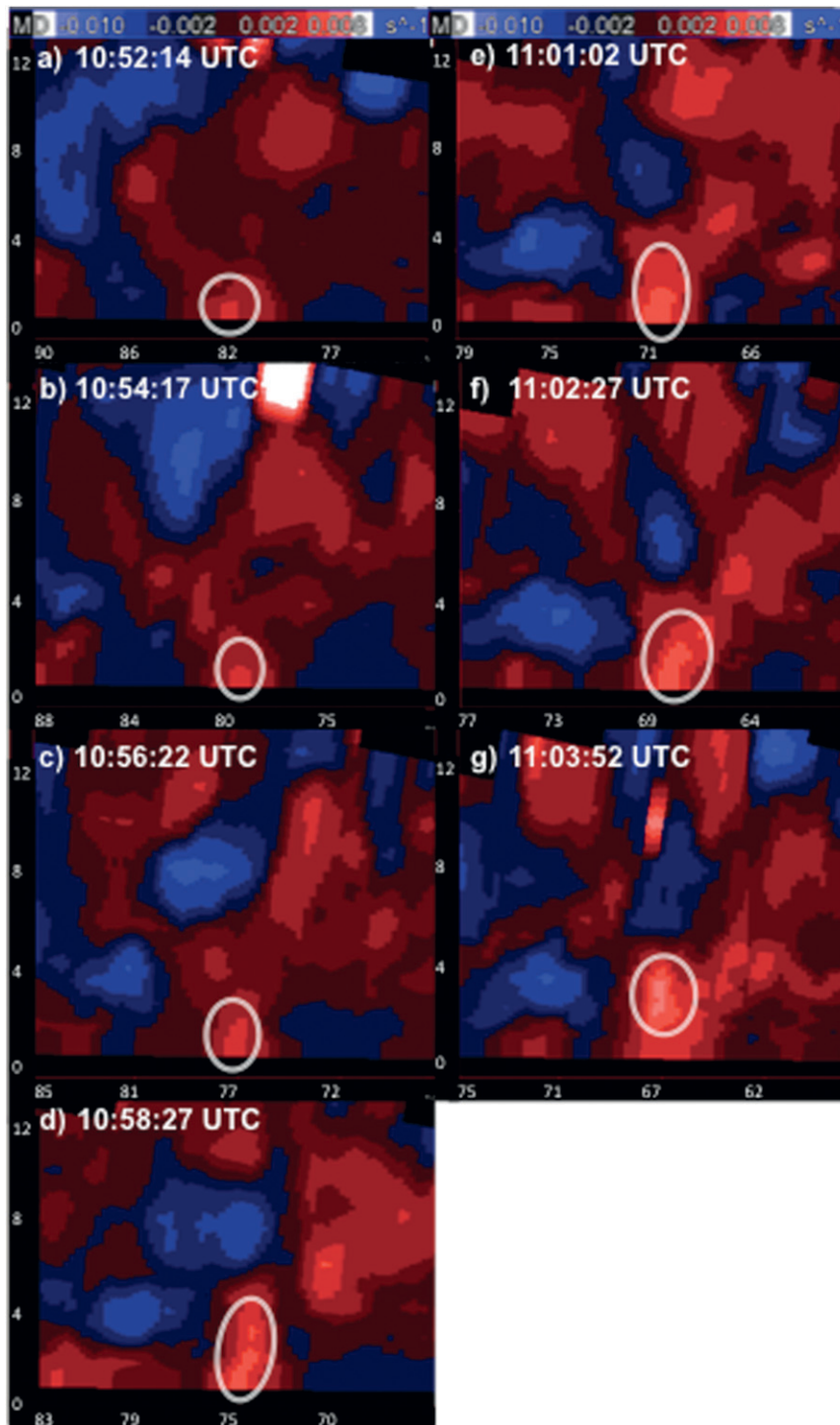


FIG. 10. PAR northeast–southwest oriented azimuthal shear vertical cross section. Shear was calculated using the LLSD method (Smith and Elmore 2004). Location of cross section at 1101 UTC shown in Fig. 9. Cross section was centered on azimuthal shear maximum and taken along the radar beam axis. Decreasing numbers on the x axis indicate distance from the PAR in km. White oval indicates approximate region where azimuthal shear exceeds 0.002 s^{-1} . (a) 1052:14, (b) 1054:17, (c) 1056:22, (d) 1058:27, (e) 1101:02, (f) 1102:27, and (g) 1103:52 UTC.

verified by Atkins and St. Laurent (2009), who discovered that in model simulations, the strongest mesovortices formed along gust fronts that were strengthened by a descending RIJ.

It is possible that in the 2 April 2010 case, the midlevel jet played a similar role to the RIJ of the Atkins et al. (2005) study. Like the tornadic mesovortices studied by Atkins et al. (2005), the Rush Springs mesovortex formed just north of the midlevel jet as the jet began to strengthen (Fig. 9) and developed from the ground up (Fig. 10). However, while Atkins et al. (2005) found that the amount of time between mesovortex genesis and tornadogenesis was 12 min, on average, for the 10 June 2003 case, PAR data suggest that the time lapse between genesis times could be much shorter (Fig. 16). More high-temporal-resolution QLCS data would need to be collected in order to substantiate this claim.

6. Comparison to KTLX and TDWR-OKC

The QLCS was also sampled by KTLX, located ~20 km northeast of the PAR, and TDWR-OKC, located ~6 km northwest of the PAR (Fig. 1). KTLX is the WSR-88D used operationally by the NWS office in Norman, Oklahoma. TDWR-OKC serves as a shear and downburst-detecting radar for airports in the Oklahoma City area and is also used operationally by the Norman NWS. Both radars sampled the Rush Springs circulation with different temporal and azimuthal resolution than the PAR. In the following sections, key features of the QLCS, as depicted in the PAR data from the event, will be compared to the depictions of these features by KTLX and TDWR.

a. KTLX and TDWR sampling strategies

KTLX is an S-band (10 cm) radar with a beamwidth of ~0.89°. KTLX collects data with an azimuthal sampling interval of 0.5° at the two lowest elevation angles and has an effective beamwidth of ~1.02° at these elevation angles, as a result of antenna rotation (Brown et al. 2002). At higher elevation angles, the effective beamwidth is ~1.4°. The KTLX range resolution is 250 m.

KTLX was operating continuously throughout the event and used two different scanning strategies. The first, volume coverage pattern (VCP) 11, collects data at 14 elevation angles and uses two PRTS for the lowest two elevation angles and one PRT for all other elevation angles (Brown et al. 2005). At approximately 1115 UTC, when the QLCS was located ~65 km from KTLX, the scanning strategy was switched to VCP 12 (Brown et al. 2005). VCP 12 also uses 14 elevation angles, but more elevation angles are focused on the lowest portion of the atmosphere. The volumetric update times for VCP 11 and 12 are approximately 5 and 4 min, respectively.

In contrast to KTLX and PAR, TDWR-OKC (hereafter TDWR) is a C-band (5 cm) radar. TDWR only provides Doppler velocity information out to 90 km in range; thus, TDWR data are only available for the Rush Springs storm starting at approximately 1100 UTC, when the circulation was already causing damage in Rush Springs. Consequently, the majority of the radar comparisons in this work focus on PAR and KTLX.

TDWR has a beamwidth of 0.55°, but the azimuthal resolution is spoiled to 1° because of a lack of processing power. The TDWR range resolution is 150 m (NWS Office of Science and Technology 2005). On 2 April 2010, TDWR was operating in hazardous mode, which is used when potentially severe storms are in range. Each hazardous mode scan consists of one long-range scan to properly place echoes in range and two volumetric scans (with elevation angles ranging from 0.5° to 28.2°). Scans at the 0.5° elevation angle are interlaced with the volumetric updates, so that data at the lowest elevation angle are available every 1 min. Each hazardous mode scan takes ~6 min (NWS Office of Science and Technology 2005).

b. Microburst: PAR and KTLX

PAR sampled the descending reflectivity core associated with the damage-producing microburst in great detail with six volumetric scans from 1037 to 1050 UTC (Fig. 5). In contrast, KTLX only sampled the microburst process with three volumetric scans during this period (Fig. 12). As a result, the descent of the reflectivity core was only visible on one scan (Fig. 12b). Examination of the 1037 and 1042 UTC scans (Figs. 12a,b) suggests the descent of high velocity from the midlevel jet toward the ground. By the next scan, at 1047 UTC, the reflectivity core had already descended to the ground and was likely causing surface wind damage (Fig. 12c). This temporal sampling limitation was also discussed by Heinselman et al. (2008) for another microburst event.

In addition, the location and time of the damage reports did not entirely correspond to the microburst signatures sampled by KTLX. For example, the golf ball-sized hail report at 1050 UTC was collocated with the reflectivity core as seen in the PAR data (Fig. 5f). This hail report occurred between KTLX scans; thus, the reflectivity core was only sampled by KTLX before (Fig. 12c) and after (not shown) the hail report time. Although it is possible that these damage reports are slightly misplaced in space and/or time (e.g., Witt et al. 1998), PAR data suggest that this is not the case (Fig. 5).

c. Midlevel jet: PAR and KTLX

The midlevel jet was not as well sampled by KTLX in comparison to PAR, largely as a result of coarser vertical sampling. KTLX employed the VCP 11 scanning

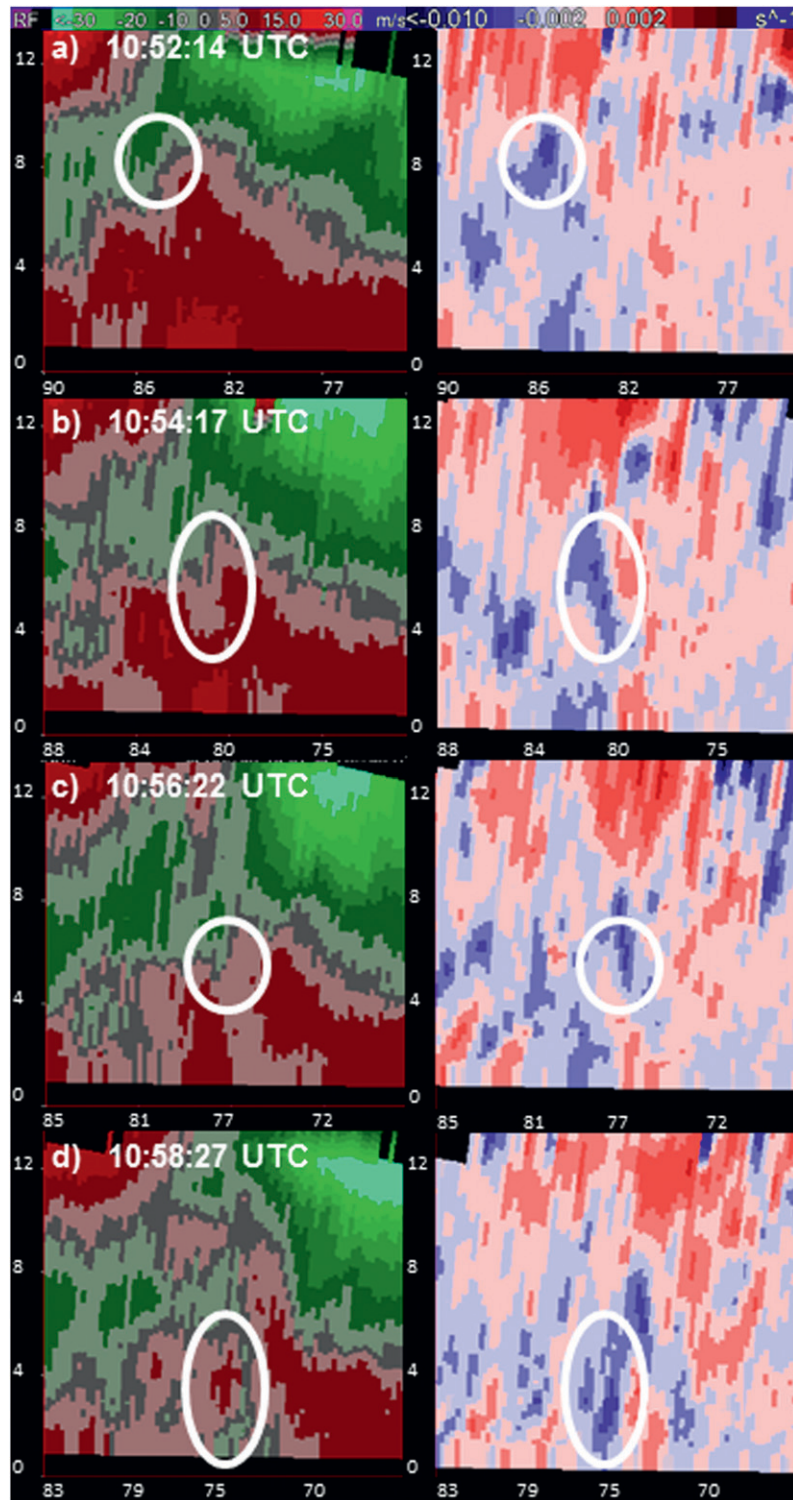


FIG. 11. PAR northeast-southwest-oriented storm-relative (left) motion and (right) divergence vertical cross sections. Location of cross section at 1101 UTC shown in Fig. 9. Cross section was centered on azimuthal shear maximum and taken along the radar beam axis. Decreasing numbers on the x axis indicate distance from the PAR in km. Divergence was calculated using the LLS method (Smith and Elmore 2004). White oval indicates approximate region where divergence is less than $-0.001 s^{-1}$. (a) 1052:14, (b) 1054:17, (c) 1056:22, (d) 1058:27, (e) 1101:02, (f) 1102:27, and (g) 1103:52 UTC.

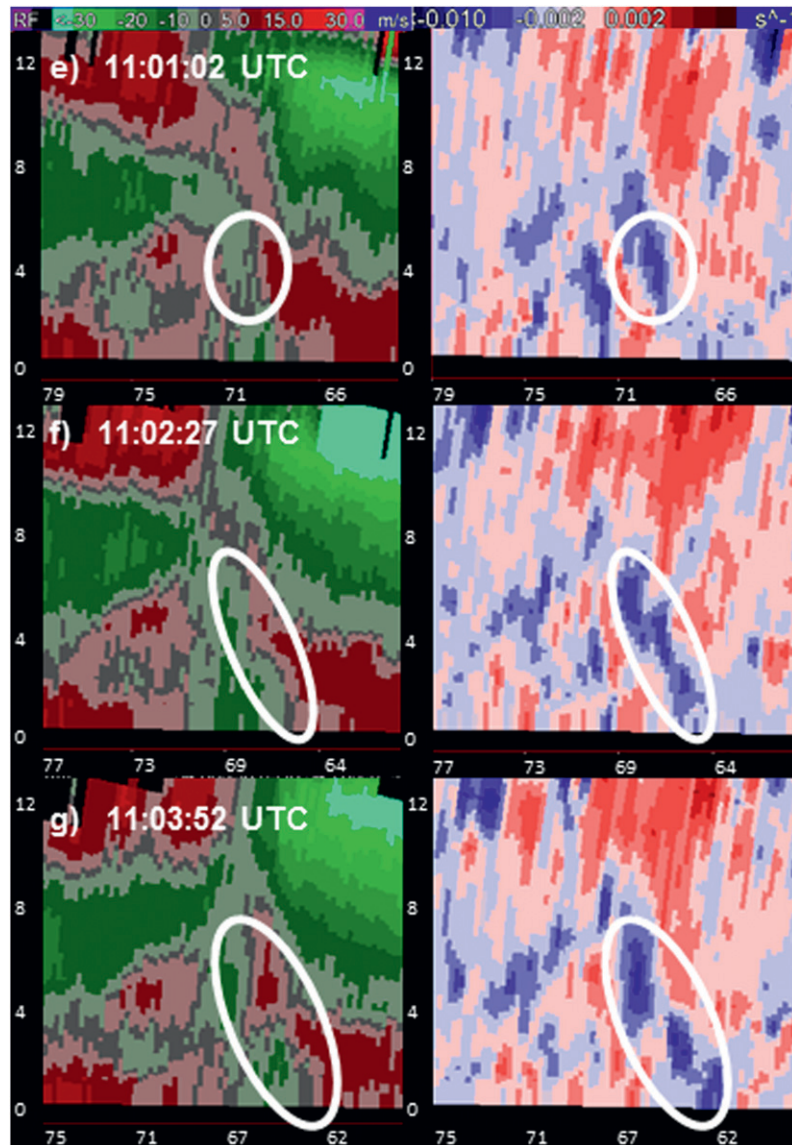


FIG. 11. (Continued)

strategy until 1115 UTC, which only features three elevation angles below 3° ; in contrast, the scanning strategies employed by the PAR collected data at six elevation angles below 3° . This difference in vertical sampling is evident in vertical cross sections from KTLX and PAR (Fig. 13). The midlevel jet and lowest part of the storm were sampled at eight elevation angles in the 1052 UTC PAR scan, compared to only four elevation angles in the corresponding KTLX scan. In the 1052 UTC cross section (Fig. 13b), the strongest region of the midlevel jet (storm-relative velocities exceeding 10 m s^{-1}) was visible in the PAR data near $x \sim 100 \text{ km}$, $z \sim 5\text{--}8.5 \text{ km}$. In contrast, the strongest part of the jet was only visible in the KTLX data near $x \sim 126 \text{ km}$, $z \sim 5.5\text{--}8 \text{ km}$ (Fig. 13a);

the jet core appeared shallower based on the coarser KTLX data. In summary, while both PAR and KTLX measured similar storm-relative velocity values in the midlevel jet, the vertical extent of the jet was resolved better in the PAR data.

*d. Mesovortex circulation and enhancement:
PAR, KTLX, and TDWR*

The velocity couplet associated with the mesovortex was evident in the KTLX data, but the evolution of the azimuthal shear maximum was not depicted in great detail. Figure 14 shows a KTLX azimuthal shear cross section taken along the path of the velocity couplet,

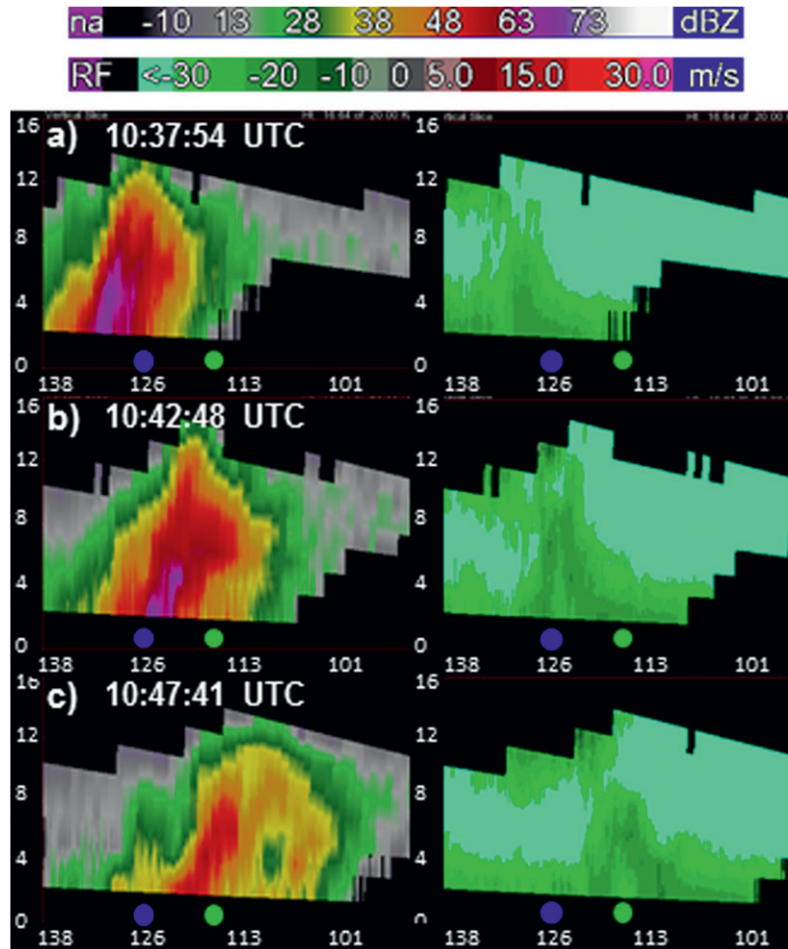


FIG. 12. As in Fig. 5, but for KTLX radar. Decreasing numbers on the x axis indicate distance from KTLX in km. (a) 1037:54, (b) 1042:48, and (c) 1047:41 UTC.

analogous to the PAR cross sections in Fig. 10. Between 1052 and 1104 UTC, KTLX completed three full volume scans, compared to seven PAR volume scans in the same time period. While the PAR data show the circulation strengthen, grow in height, and subsequently weaken, the evolution is not as clear in the KTLX data.

A time series of maximum low-level LLSD azimuthal shear values derived from all three central Oklahoma radars before, during, and after the Rush Springs damage time period (Fig. 15a) further illustrates this point. [Shear was calculated using the local, linear least squares derivatives (LLSD) method (Smith and Elmore 2004). Note that it is the trends in azimuthal shear, rather than the actual values, that are important in this case, since LLSD shear values can vary according to range, radar angle, and beamwidth (Smith and Elmore 2004).] The PAR data indicate a gradual increase in azimuthal shear from 1052 to 1101 UTC, followed by a slight decrease and another increase at 1106 UTC as the circulation

appeared to reintensify. This reintensification appeared to occur as the leading edge of the midlevel jet strengthened and began to slope down toward the leading edge of the QLCS, creating another area of deep, strong convergence (not shown). TDWR, which used low-level temporal resolution that was similar to PAR, displayed similar trends in the azimuthal shear field. The KTLX data do not show the evolution of these two azimuthal shear maxima.

Figure 15b shows the temporal evolution of the maximum low-level velocity difference measured by all three radars. In general, the velocity difference showed a similar temporal trend to the azimuthal shear—an increase until 1101 UTC, followed by a slight decrease and another increase at 1106 UTC. However, the TDWR velocity difference values are significantly higher than the PAR and KTLX values at nearly every scan time. In addition, some of the TDWR values represent gate-to-gate velocity differences (e.g., 34 m s^{-1} at 1108 UTC), while the PAR

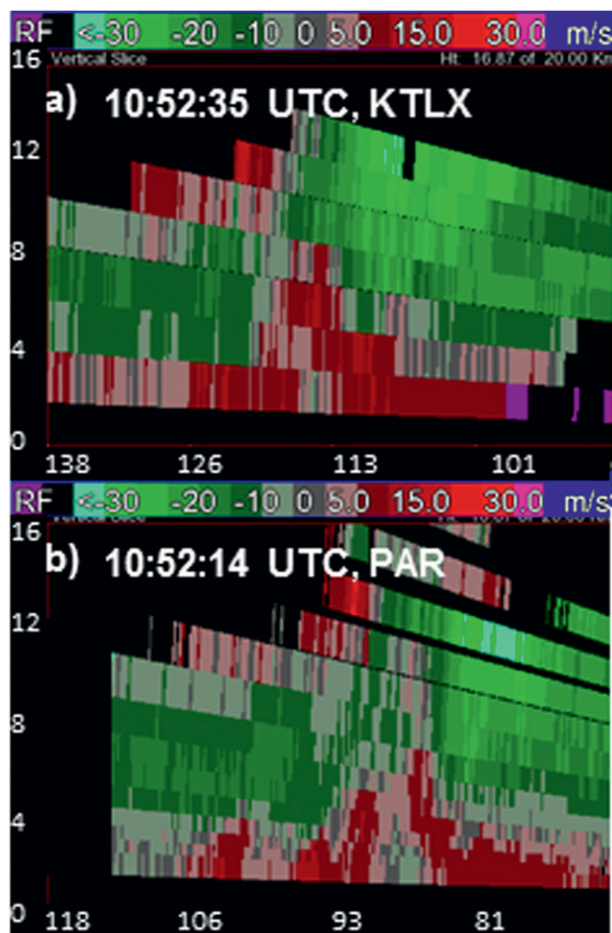


FIG. 13. KTLX and PAR northeast-southwest storm-relative motion vertical cross sections. Location of cross section shown in Fig. 4. Decreasing numbers on the *x* axis indicate decreasing distance from the radars in km. Times refer to time of 0.5° elevation scan. (a) KTLX, 1052:35 UTC and (b) PAR, 1052:14 UTC.

and KTLX maximum and minimum velocities were separated by at least one azimuth. This discrepancy is likely due to the difference in beamwidth between TDWR and PAR. TDWR uses a 1° beamwidth with 150-m range resolution while the PAR beamwidth was ~1.6° at the circulation location with a 240-m range resolution. TDWR was likely sampling the small-scale, stronger circulation while PAR was sampling the larger-scale, surrounding circulation. KTLX, with an effective beamwidth of ~1.02° and a range resolution of 250 m, sampled similar velocity difference values to PAR.

7. Summary and conclusions

The NWRT PAR sampled the 2 April 2010 QLCS as damage equivalent to an EF1-scale tornado was occurring in Rush Springs, Oklahoma. This damage appeared

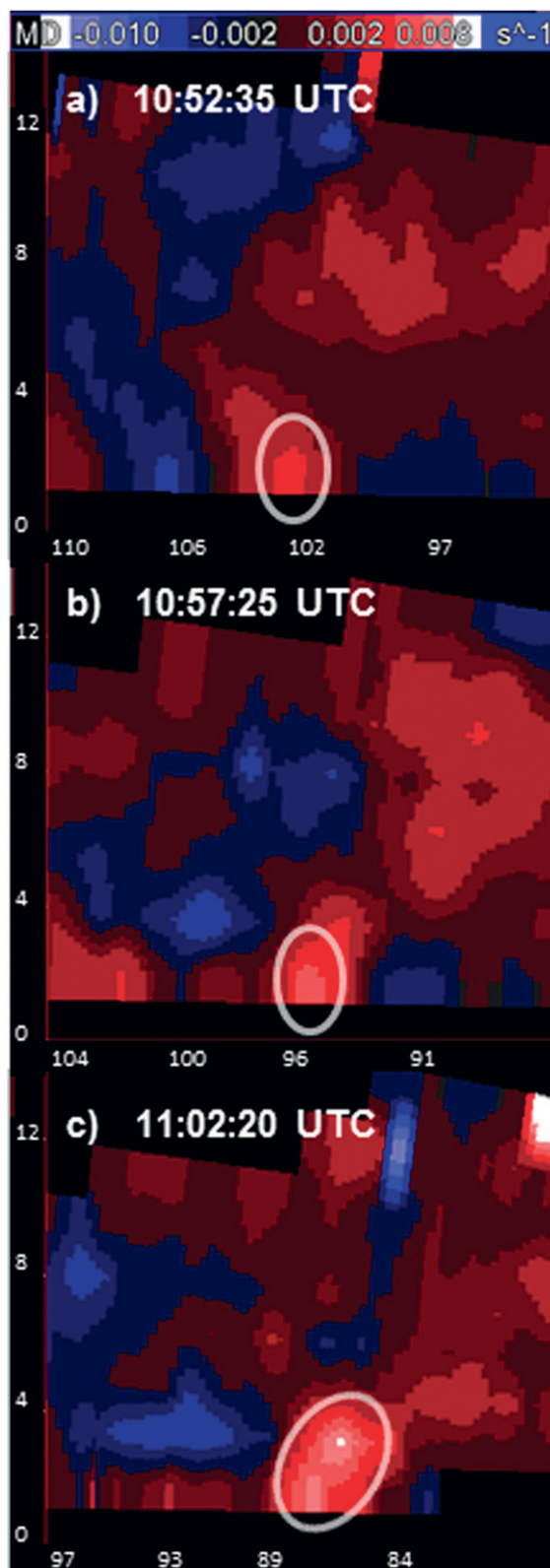


FIG. 14. As in Fig. 10, but for KTLX azimuthal shear. Decreasing numbers on the *x* axis indicate distance from KTLX in km. (a) 1052:35, (b) 1057:25, and (c) 1102:20 UTC.

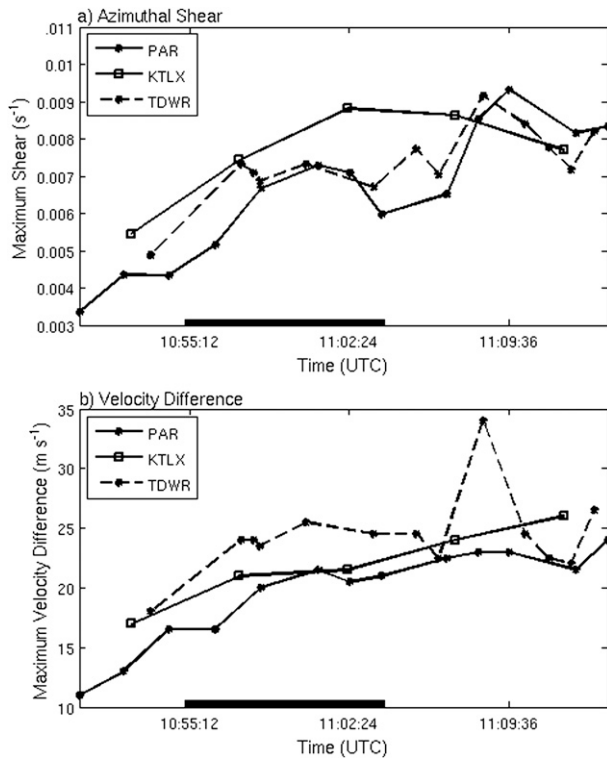


FIG. 15. Time series of maximum 0.5° (a) azimuthal shear and (b) velocity difference values along circulation path from PAR, KTLX, and TDWR data. Maximum velocity difference was found by calculating the difference between the maximum and minimum velocity values at constant range within a 3-km search radius of each point. Black line indicates approximate circulation damage period. At 1102 UTC, the 0.5° elevation angles of PAR, KTLX, and TDWR were sampling the circulation at 0.9, 1.2, and 0.9 km ARL, respectively.

to be associated with a mesovortex that developed and strengthened along the leading edge of the QLCS. Full-volume scans were completed by the PAR approximately every 2 min or less, revealing the evolution of the QLCS in great detail. In addition, the PAR used a scanning strategy with high vertical resolution, collecting data at 22 elevation angles, compared to only 14 elevation angles used by the nearby WSR-88D in Twin Lakes, Oklahoma.

The evolution of the QLCS as it approached Rush Springs and began producing EF1-scale damage is summarized in Fig. 16. As observed in the PAR data, the microburst high-reflectivity core reached the ground at approximately 1044 UTC. The microburst appeared to signify the first in a series of momentum transfers from the strengthening midlevel jet to the ground at several points along the QLCS; as a result of these momentum transfers, a region of strong low-level outflow developed northwestward along the QLCS, eventually reaching the location of the Rush Springs circulation. The PAR data

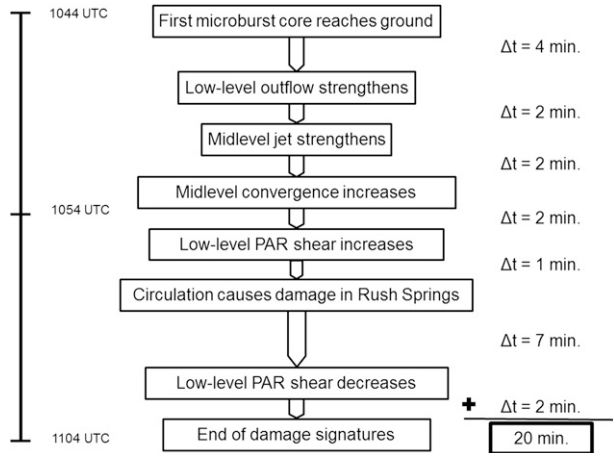


FIG. 16. Diagram depicting evolution of Rush Springs circulation as observed in PAR data. Time increases toward the bottom of the diagram; Δt is the time elapsed between the start times of subsequent radar-indicated signatures.

suggest that this high momentum may have provided the strong convergence necessary to strengthen the preexisting mesovortex and cause damage in Rush Springs. At 1052 UTC, the midlevel convergence began to increase substantially in response to the strengthening jet. Two minutes later, the low-level shear calculated with the PAR data began to increase, nearly doubling between 1054 and 1101 UTC. One minute after the low-level shear began to increase, the circulation started causing damage in Rush Springs; the circulation continued to cause damage at the surface for the next 9 min. The entire process, from the descent of the microburst core to the end of the wind damage associated with the circulation, took place in approximately 20 min.

The rapid evolution of this event highlights the advantages of using rapid-scan volumetric radar data to depict trends in potentially damaging storms. In addition, we suggest that monitoring midlevel features, such as a midlevel jet or RIJ, requires a vast amount of volumetric data not available with the current WSR-88D network. The increased availability of volumetric PAR data ensured that the strengthening midlevel jet was well resolved and observed in great detail. The PAR data also depicted a descending reflectivity core associated with a microburst and an intensifying azimuthal shear maximum associated with the mesovortex. Both these events occurred on very short time scales (5 min or less) and were therefore not depicted in great detail by KTLX.

Data collected by the PAR for the Rush Springs event revealed several potential precursors for damaging circulation formation in QLCSs, such as a strengthening midlevel jet and strong midlevel convergence. In the future, more rapid-scan volumetric radar data collected

on QLCS cases could further advance the knowledge of mesovortex formation and highlight additional radar precursors for QLCS circulations.

Acknowledgments. The authors thank Rick Hluchan for monitoring PAR data collection for the event, Kevin Manross for assisting with acquisition of TDWR data, Kiel Ortega for supplying damage survey information, Ami Arthur for assisting with figures, and Jeff Brogden for assisting with PAR data conversion. Conversations with Dave Andra, Mike Coniglio, and Dusty Wheatley aided our radar data analysis. Comments from three anonymous reviewers helped improve the quality of the manuscript. The authors would also like to acknowledge the developers of NCAR's Solo II radar data editing program and Dennis Flanigan, the developer of the PAR data translator for Solo II. Funding for the first author was provided by NOAA/Office of Oceanic and Atmospheric Research under NOAA–University of Oklahoma Cooperative Agreement NA17RJ1227, U.S. Department of Commerce.

REFERENCES

- Ashley, W. S., A. J. Krmenc, and R. Schwantes, 2008: Vulnerability due to nocturnal tornadoes. *Wea. Forecasting*, **23**, 795–807.
- Atkins, N. T., and M. St. Laurent, 2009: Bow echo mesovortices. Part II: Their genesis. *Mon. Wea. Rev.*, **137**, 1514–1532.
- , C. S. Bouchard, R. W. Przybylinski, R. J. Trapp, and G. Schmocker, 2005: Damaging surface wind mechanisms within the 10 June 2003 Saint Louis Bow Echo during BAMEX. *Mon. Wea. Rev.*, **133**, 2275–2296.
- Brotzge, J., and S. Erickson, 2010: Tornadoes without NWS warning. *Wea. Forecasting*, **25**, 159–172.
- Brown, R. A., V. T. Wood, and D. Sirmans, 2002: Improved tornado detection using simulated and actual WSR-88D data with enhanced resolution. *J. Atmos. Oceanic Technol.*, **19**, 1759–1771.
- , —, R. M. Steadham, R. R. Lee, B. A. Flickinger, and D. Sirmans, 2005: New WSR-88D volume coverage pattern 12: Results of field tests. *Wea. Forecasting*, **20**, 385–393.
- Davis, C., and Coauthors, 2004: The Bow Echo and MCV Experiment: Observations and opportunities. *Bull. Amer. Meteor. Soc.*, **85**, 1075–1093.
- Doswell, C. A., III, 2001: Severe convective storms: An overview. *Severe Convective Storms, Meteor. Monogr.*, No. 50, Amer. Meteor. Soc., 1–26.
- Evans, J. S., and C. A. Doswell, 2001: Examination of derecho environments using proximity soundings. *Wea. Forecasting*, **16**, 329–342.
- Forbes, G. S., and R. M. Wakimoto, 1983: A concentrated outbreak of tornadoes, downbursts and microbursts, and implications regarding vortex classification. *Mon. Wea. Rev.*, **111**, 220–236.
- Fujita, T. T., 1971: Proposed characterization of tornadoes and hurricanes by area and intensity. SMRP Research Paper 91, University of Chicago, Chicago, IL, 42 pp.
- , 1978: Manual of downburst identification for Project NIMROD. SMRP Research Paper 156, University of Chicago, Chicago, IL, 104 pp.
- , 1981: Tornadoes and downbursts in the context of generalized planetary scales. *J. Atmos. Sci.*, **38**, 1511–1534.
- Heinzelman, P. L., and S. M. Torres, 2011: High-temporal-resolution capabilities of the National Weather Radar Testbed Phased-Array Radar. *J. Appl. Meteor. Climatol.*, **50**, 579–593.
- , D. L. Priegnitz, K. L. Manross, T. M. Smith, and R. W. Adams, 2008: Rapid sampling of severe storms by the National Weather Radar Testbed Phased Array Radar. *Wea. Forecasting*, **23**, 808–824.
- Heymsfield, G. M., and S. Schotz, 1985: Structure and evolution of a severe squall line over Oklahoma. *Mon. Wea. Rev.*, **113**, 1563–1589.
- Junyent, F., V. Chandrasekar, D. McLaughlin, E. Insanic, and N. Bharadwaj, 2010: The CASA Integrated Project 1 networked radar system. *J. Atmos. Oceanic Technol.*, **27**, 61–78.
- Maddox, R. A., 1983: Large-scale meteorological conditions associated with midlatitude, mesoscale convective complexes. *Mon. Wea. Rev.*, **111**, 1475–1493.
- Mahale, V. N., J. A. Brotzge, and H. B. Bluestein, 2012: An analysis of vortices embedded within a quasi-linear convective system using X-band polarimetric radar. *Wea. Forecasting*, in press.
- Mahoney, K. M., G. M. Lackmann, and M. D. Parker, 2009: The role of momentum transport in the motion of a quasi-idealized mesoscale convective system. *Mon. Wea. Rev.*, **137**, 3316–3338.
- McDonald, J. R., G. S. Forbes, and T. P. Marshall, 2004: The enhanced Fujita (EF) scale. Preprints, *22nd Conf. on Severe Local Storms*, Hyannis, MA, Amer. Meteor. Soc., 3B.2. [Available online at <https://ams.confex.com/ams/pdfpapers/81090.pdf>.]
- NCDC, 2010: *Storm Data*. Vol. 52, No. 4, 384 pp.
- NWS Office of Science and Technology, 2005: TDWR interface control and specifications documentation for the NWS supplemental product generator. Version 4.3, Tech. Rep., National Oceanic and Atmospheric Administration, 42 pp. [Available online at http://www.wdtb.noaa.gov/buildtraining/TDWR/TDWR_SPG_ICD_v43.pdf.]
- Oye, R., C. Mueller, and S. Smith, 1995: Software for radar translation, visualization, editing, and interpolation. Preprints, *27th Conf. on Radar Meteorology*, Vail, CO, Amer. Meteor. Soc., 359–364.
- Rasmussen, E. N., and D. O. Blanchard, 1998: A baseline climatology of sounding-derived supercell and tornado forecast parameters. *Wea. Forecasting*, **13**, 1148–1164.
- SHAVE, cited 2010: Tornado surveys map. [Available online at <http://ewp.nssl.noaa.gov/projects/shave/tornsurveys.php>.]
- Smith, T. M., and K. L. Elmore, 2004: The use of radial velocity derivatives to diagnose rotation and divergence. Preprints, *11th Conf. on Aviation, Range, and Aerospace*, Hyannis, MA, Amer. Meteor. Soc., P5.6. [Available online at <https://ams.confex.com/ams/pdfpapers/81827.pdf>.]
- Smull, B. F., and R. A. Houze, 1987: Rear inflow in squall lines with trailing stratiform precipitation. *Mon. Wea. Rev.*, **115**, 2869–2889.
- Trapp, R. J., and M. L. Weisman, 2003: Low-level mesovortices within squall lines and bow echoes. Part II: Their genesis and implications. *Mon. Wea. Rev.*, **131**, 2804–2823.
- , E. D. Mitchell, G. A. Tipton, D. W. Effertz, A. I. Watson, D. L. Andra, and M. A. Magsig, 1999: Descending and non-descending tornadic vortex signatures detected by WSR-88Ds. *Wea. Forecasting*, **14**, 625–639.
- , S. A. Tessendorf, E. S. Godfrey, and H. E. Brooks, 2005: Tornadoes from squall lines and bow echoes. Part I: Climatological distribution. *Wea. Forecasting*, **20**, 23–34.

- Wakimoto, R. M., and J. W. Wilson, 1989: Non-supercell tornadoes. *Mon. Wea. Rev.*, **117**, 1113–1140.
- , H. V. Murphey, A. Nester, D. P. Jorgensen, and N. T. Atkins, 2006a: High winds generated by bow echoes. Part I: Overview of the Omaha bow echo 5 July 2003 storm during BAMEX. *Mon. Wea. Rev.*, **134**, 2793–2812.
- , —, C. A. Davis, and N. T. Atkins, 2006b: High winds generated by bow echoes. Part II: The relationship between the mesovortices and damaging straight-line winds. *Mon. Wea. Rev.*, **134**, 2813–2829.
- Weisman, M. L., 1992: The role of convectively generated rear-inflow jets in the evolution of long-lived mesoconvective systems. *J. Atmos. Sci.*, **49**, 1826–1847.
- , 1993: The genesis of severe, long-lived bow echoes. *J. Atmos. Sci.*, **50**, 645–670.
- , and R. J. Trapp, 2003: Low-level mesovortices within squall lines and bow echoes. Part I: Overview and dependence on environmental shear. *Mon. Wea. Rev.*, **131**, 2779–2803.
- Wheatley, D. M., R. J. Trapp, and N. T. Atkins, 2006: Radar and damage analysis of severe bow echoes observed during BAMEX. *Mon. Wea. Rev.*, **134**, 791–806.
- Wilson, J., R. Carbone, H. Baynton, and R. Serafin, 1980: Operational application of meteorological Doppler radar. *Bull. Amer. Meteor. Soc.*, **61**, 1154–1168.
- Witt, A., M. D. Eilts, G. J. Stumpf, E. D. W. Mitchell, J. T. Johnson, and K. W. Thomas, 1998: Evaluating the performance of WSR-88D severe storm detection algorithms. *Wea. Forecasting*, **13**, 513–518.
- Zrnić, D. S., and Coauthors, 2007: Agile-beam phased array radar for weather observations. *Bull. Amer. Meteor. Soc.*, **88**, 1753–1766.